Angular-resolved electron energy loss spectroscopy on a split-ring resonator

F. von Cube,[1,2,3,*] J. Niegemann,[4] S. Irsen,[2] D. C. Bell,[3,5] and S. Linden[1]

[1]*Physikalisches Institut, Universität Bonn, 53115 Bonn, Germany*

[2]*Electron Microscopy and Analytics (EMA), Center of Advanced European Studies and Research (caesar), 53175 Bonn, Germany*

[3]*Center for Nanoscale Systems, Harvard University, Cambridge, Massachusetts 02138, USA*

[4]*Laboratory for Electromagnetic Fields (IFH), ETH Zurich, 8092 Zurich, Switzerland*

[5]*School of Engineering and Applied Sciences, Harvard University, Cambridge, Massachusetts 02138, USA*

(Received 22 November 2013; revised manuscript received 14 March 2014; published 26 March 2014)

We investigate the plasmonic near field of a lithographically defined split-ring resonator with angular-resolved electron energy loss spectroscopy in a scanning transmission electron microscope. By tilting the sample, different electric field components of the plasmonic modes can be probed with the electron beam. The electron energy loss spectra recorded under oblique incidence can feature plasmonic resonances that are not observable under normal incidence. Our experimental findings are supported by full numerical calculations based on the discontinuous Galerkin time-domain method.

DOI: 10.1103/PhysRevB.89.115434 PACS number(s): 79.20.Uv, 73.20.Mf

I. INTRODUCTION

Plasmonic modes in metallic nanostructures provide a unique route to concentrate electromagnetic fields in deep-subwavelength volumes. The local intensity in the vicinity of the nanostructures can exceed the incident light intensity by orders of magnitude. This effect can lead to an enhanced light-matter interaction and is an important motivation for various research activities in the field of plasmonics, e.g., for plasmonic sensing applications [1], optical antennas [2], nonlinear plasmonics [3], and quantum plasmonics [4].

The experimental characterization of plasmonic near-field distributions requires spectroscopic methods that provide nanometer-scale spatial resolution. Recent experiments have shown that electron energy loss spectroscopy (EELS) in a scanning transmission electron microscope (STEM) is particularly suited for this purpose. In STEM-EELS, a tightly focused electron beam is raster scanned across the metallic nanostructure and the energy loss of the transmitted electrons due to the excitation of a plasmonic mode is recorded for each beam position. Alternatively, an energy filtering TEM (EFTEM) with a broad electron beam can be used to directly acquire a complete EELS map by imaging only those electrons which experienced a specific energy loss. Both techniques have been applied to map the plasmonic modes of a variety of metallic nanostructures such as nanotriangles [5,6], nanorods and nanowires [7,8], dimer structures [9–11], bowtie antennas [12], nanodisks [13], split-ring resonators [14–16], and apertures in metal films [17].

For planar metallic nanostructures, antinodes of the plasmonic charge density oscillations usually appear as pronounced maxima in the corresponding EEL maps. In contrast, hot spots in the gaps between plasmonic particles – as in the case of the bonding mode of a plasmonic dimer – do not give rise to strong EELS signals for normal incidence of the electron beam [9–11,18]. Both observations can be easily explained by taking into account the influence of the excitation geometry on the EELS signal. Consider an incident fast electron that excites one of the plasmonic modes of a planar metallic nanostructure under normal incidence. The induced electric field $\mathbf{E}_{\mathrm{ind}}$ of the excited plasmonic mode acts back on the electron and, as a result, the electron experiences an energy loss ΔE equal to the energy $\hbar\omega_{\mathrm{pl}}$ of the excited plasmonic mode. In this process, the energy loss ΔE and the loss probability $\Gamma_{\mathrm{EELS}}(\omega)$ are related [19–21] via

$$\Delta E = e\int \mathbf{v}\cdot\mathbf{E}_{\mathrm{ind}}[\mathbf{r}_{\mathrm{e}}(t),t]dt = \int_0^\infty \hbar\omega\,\Gamma_{\mathrm{EELS}}(\omega)d\omega, \quad (1)$$

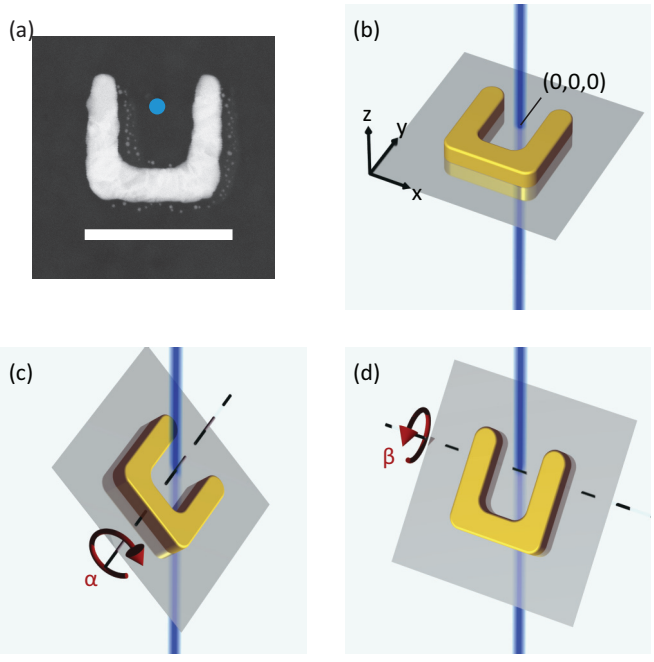

FIG. 1. (Color online) (a) Dark-field image of a split-ring resonator. The blue dot marks the position of the electron beam. The length of the scale bar is 200 nm. (b) Schematic view of the SRR and the electron beam (blue line) for normal incidence. In (c) the sample is rotated around the y axis by $\alpha = 46^\circ$, and in (d) the sample is rotated around the x axis by $\beta = 46^\circ$.

*voncube@uni-bonn.de

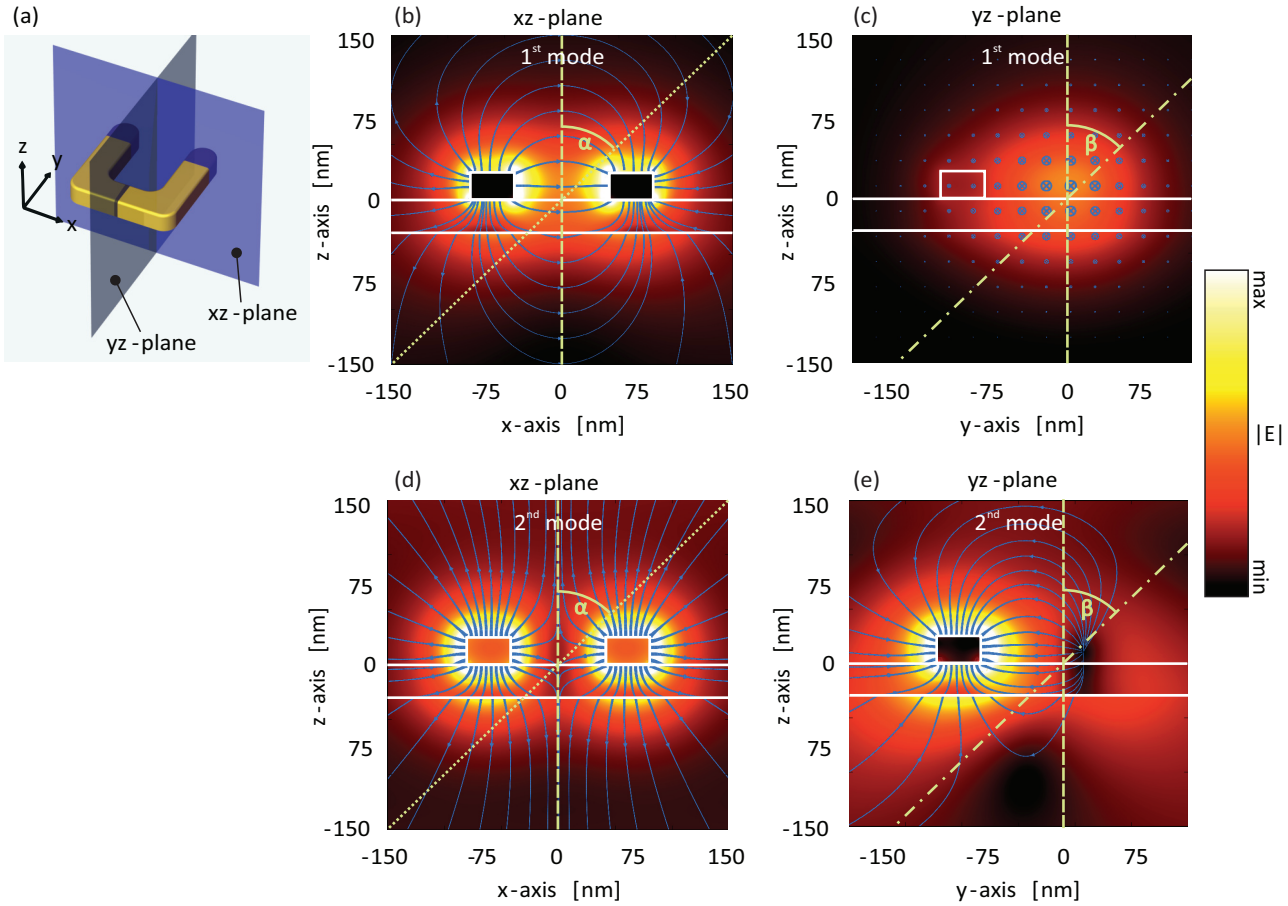

FIG. 2. (Color online) Calculated near-field distribution of the first- and second-order mode of a split-ring resonator. (a) shows the two planes relevant for the experiments. (b) depicts the electric field of the first mode in the xz plane at $y = 0$; the blue lines indicate the electric field lines and the color represents the modulus of the electric field $|\mathbf{E}|$. For $x = 0$, all field lines are oriented horizontally and point in one direction. (c) shows the electric field within the yz plane ($x = 0$) of the first mode; the electric field lines are perpendicular to this plane, as indicated by blue crosses. (d) and (e) show the electric field distribution of the second-order mode in the xz and yz planes, respectively. The solid white lines are the boundaries of the membrane and the SRR. The dashed, the dotted, and the dashed-dotted line represent the electron trajectories for $\alpha = \beta = 0^\circ$, $\alpha = 46^\circ$, and $\beta = 46^\circ$, respectively.

where $-e$ and $\mathbf{v}$ are the charge and the velocity of the electron, respectively, and $\mathbf{r}_e(t)$ is its trajectory. The loss probability $\Gamma_{\mathrm{EELS}}(\omega)$ can be expressed as

$$\Gamma_{\mathrm{EELS}}(\omega) = \frac{e}{\pi\hbar\omega}\int \mathrm{Re}(e^{-i\omega t}\mathbf{v}\cdot\mathbf{E}_{\mathrm{ind}}[\mathbf{r}_e(t),\omega])dt, \qquad (2)$$

where $\mathbf{E}_{\mathrm{ind}}[\mathbf{r},\omega]$ is the Fourier transform of $\mathbf{E}_{\mathrm{ind}}[\mathbf{r},t]$. Inspection of Eq. (2) immediately shows that only the component of $\mathbf{E}_{\mathrm{ind}}[\mathbf{r},\omega]$ parallel to $\mathbf{v}$, and thus parallel to the electron trajectory, is relevant for the loss probability. The antinodes of the plasmonic charge density oscillation of a planar metallic nanostructure usually give rise to a local electric field that has a significant component parallel to the electron beam. Thus, we can expect a large EELS signal if the electron beam is focused on one of these antinodes. In contrast, $\Gamma_{\mathrm{EELS}}(\omega)$ is very small if the plasmonic near field is predominately oriented orthogonal to the electron trajectory. This situation corresponds, e.g., to the case of the bonding mode of a plasmonic dimer if the electron beam passes the gap between the two particles under normal incidence.

In this paper, we perform angular-resolved EELS to show that whether or not a plasmonic hot spot can be seen in EELS depends on the excitation geometry. For this purpose, we use a split-ring resonator (SRR) as a model system [see Fig. 1(a)]. Its first plasmonic mode exhibits a hot spot in the region between the two tips (see Fig. 2). There, the field distribution closely resembles the field distribution of the bonding mode in the gap of a plasmonic dimer. However, the spectral overlap between the first plasmonic mode and the second plasmonic mode is significantly smaller in the case of the SRR. This is a distinct advantage of the SRR compared to the plasmonic dimer for the intended experiments. EELS maps of the first SRR mode recorded under normal incidence feature very small signals in the region of the hot spot [14–16]. We will show that by performing oblique incidence EELS, we can probe different electric field components of the plasmonic mode with the electron beam and thus "cure the blindness of EELS to hot spots".

In a recent theoretical analysis, it was shown that a set of oblique incidence EELS maps can in principle even be used to fully reconstruct the three-dimensional plasmonic

near field [22]. Corresponding experiments were presented in Ref. [23]. Here, we refrain from a quantitative reconstruction of the plasmonic near field since the proposed scheme relies on the quasistatic approximation which is not applicable for SRRs of our size [24].

II. METHODS

The SRR depicted in Fig. 1(a) was fabricated by standard electron-beam lithography on a 30 nm thin Si_3N_4 membrane. A 2 nm thin chromium layer served as an adhesion layer for the 25 nm thin gold film. For the STEM-EELS experiments, we used a Zeiss Libra200 STEM microscope equipped with a monochromator, a Cs corrector, and an in-column Ω-type energy filter. The acceleration voltage was set to 80 kV. By working with this relatively low accelerating voltage, we achieved an energy resolution as defined by the full width at half maximum (FWHM) of the zero loss peak on the bare substrate of only 90 meV. To increase the signal-to-noise ratio, we recorded 40 individual spectra at each position. The acquisition time per spectrum was 0.3 s. Before averaging, the zero loss peak of each spectrum was centered at 0 eV. Further details of the fabrication method, the measurement, and the normalization procedure can be found in Ref. [15].

III. RESULTS

In the first step, an electron energy loss spectrum was recorded under normal incidence at one tip of the SRR (not shown). The resonance energies of the first and the second plasmonic mode of the SRR derived from this spectrum were 0.69 and 1.19 eV, respectively. Next, the sample was rotated from $\alpha = 0^\circ$ to $\alpha = 46^\circ$ in steps of 1° around the y axis [see Fig. 1(c)]. Larger rotation angles led to a blocking of the electron beam by the silicon frame that supports the Si_3N_4 membrane. For each angle of incidence, an electron energy loss spectrum was recorded at the center between the two tips of the SRR [see the blue dot in Fig. 1(a)]. Figure 3(a) depicts this series of electron energy loss spectra. For normal incidence ($\alpha = 0^\circ$), we do not find a signature of the first plasmonic mode since its electric field is predominately oriented parallel to the substrate in the gap. However, for oblique incidence, a peak emerges at the spectral position of the first plasmonic mode that continuously gains in strength with increasing α. This is in accordance with our expectations as the angle enclosed between the electron trajectory and the electric field lines of the first plasmonic mode in the region between the tips becomes smaller with increasing α. The second plasmonic mode at 1.19 eV is clearly visible even for normal incidence since its electric field distribution has a nonvanishing component along the electron trajectory [see Figs. 2(d) and 2(e)]. With an increasing angle of incidence, the intensity of the second plasmonic mode grows as well. However, this effect is less pronounced for the second plasmonic mode than for the first plasmonic mode. Therefore, for large values of α, the first plasmonic mode becomes the dominant spectral feature.

Within our experimental accuracy, the resonance energies of the two plasmonic modes do not shift with the angle of incidence and are identical to the values determined at the tips of the SRR for normal incidence. The depicted spectra

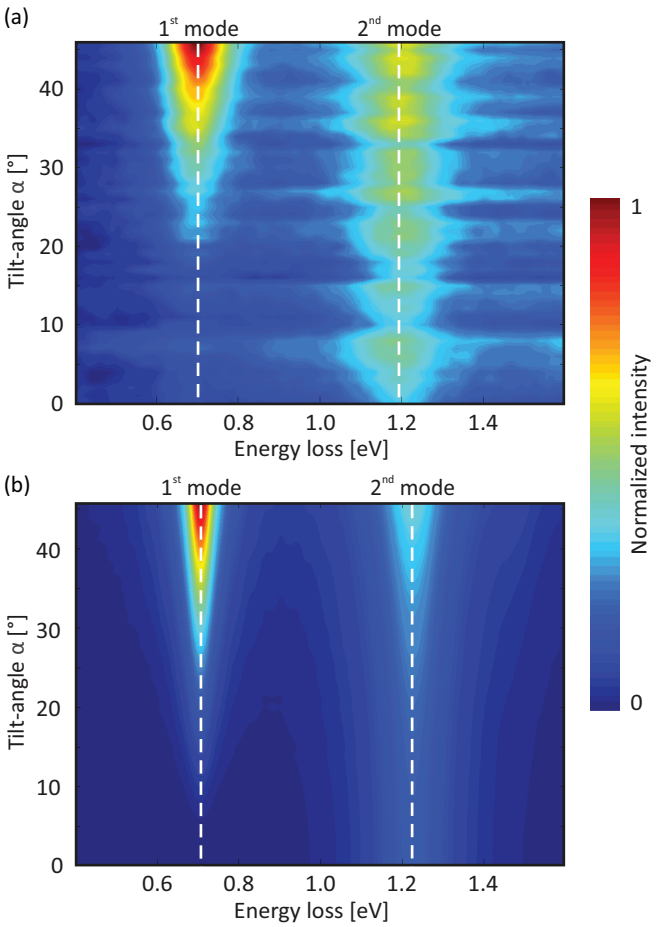

FIG. 3. (Color online) (a) Measured oblique incidence electron energy loss spectra recorded between the two tips of a split-ring resonator for different tilt angles around the y axis. (b) Corresponding calculated electron energy loss spectra. The dashed lines indicate the resonance energy of the first and the second plasmonic mode, respectively.

were recorded for positive tilt angles. As might be expected from the symmetry of the SRR, within our experimental accuracy we find identical trends also for negative tilt angles (not shown). The horizontal features in the contour plot are artifacts which stem from periodic cleaning of the sample in an oxygen plasma to remove carbonaceous contamination caused by the illumination with the electron beam. The first cleaning of the sample with an oxygen plasma prior to the EELS experiments can result in a small blueshift of the resonances [25]. This can probably be traced back to the removal of organic residues from the fabrication process. However, subsequent treatments with the oxygen plasma have no observable effect on the resonance frequencies.

Our experiments are compared with numerical calculations based on an in-house implementation of the nodal discontinuous Galerkin time-domain (DGTD) algorithm (see Ref. [26] and references therein). This technique allows efficient time-domain calculations in complex systems and was shown to be well suited for the accurate simulation of plasmonic nanostructures. For the computation of the electron energy loss spectra from the simulation data, we follow the

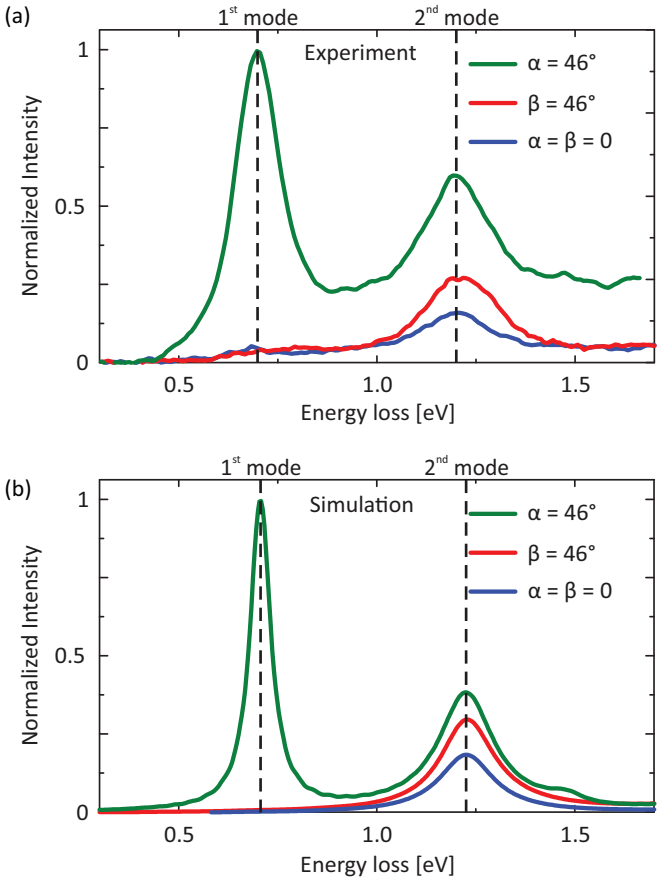

FIG. 4. (Color online) (a) Measured electron energy loss spectra recorded between the two tips of the split-ring resonator [see the blue dot in Fig. 1(a)] for normal and oblique incidence for different axes of rotation. (b) Corresponding calculated electron energy loss spectra.

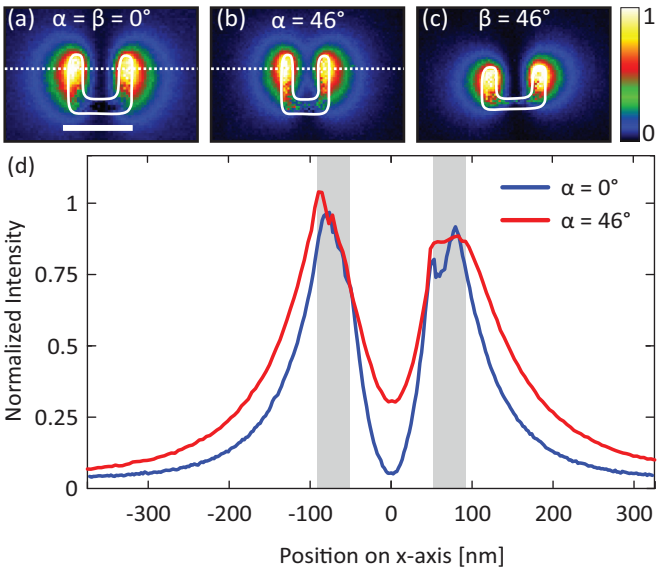

FIG. 5. (Color online) EELS maps of the SRR depicted in Fig. 1(a) at an energy loss of 0.69 eV for three different tilt angles for (a) $\alpha = 0°, \beta = 0°$, (b) $\alpha = 46°, \beta = 0°$, and (c) $\alpha = 0°, \beta = 46°$. The solid white lines indicate the boundaries of the SRR. The scale bar is 200 nm. (d) Line scans of the electron beam along the x axis [dashed lines in (a) and (b)]. The gray areas represent the positions of the SRR tips for $\alpha = 0°$.

approach discussed in Ref. [27] with extensions discussed in Refs. [15,16]. Since the DGTD method is a time-domain approach, we employ auxiliary differential equations to model the dispersive behavior of gold. More specifically, we use a Drude-Lorentz model with the parameters stated in Ref. [27]. The dimensions of the simulated SRR were taken from the scanning electron micrograph [see Fig. 1(a)]. Small deviations of the actual fabricated structure from the ideal shape were neglected. Figure 3(b) depicts the calculated electron energy loss spectra for the same conditions as in the experiments. The numerical calculations nicely reproduce the experimental results. In accordance with the experimental data, we observe in the calculated data a dramatic increase of the intensity of the first plasmonic mode (at 0.71 eV) and only a slight increase of the intensity of the second plasmonic mode (at 1.22 eV) with increasing angle.

We performed a control experiment in which we rotated the sample around the x axis by $\beta = 46°$ [see Fig. 1(d)]. In this case, the electron trajectory lies in the yz plane and, hence, is normal to the electric field lines of the first plasmonic mode in the region between the tips [see Fig. 2(c)]. The red curve in Fig. 4(a) depicts the corresponding electron energy loss spectrum recorded at the same position as in the previous experiment. In accordance with our expectations, the first plasmonic mode is absent in this spectrum. This finding is also reproduced by numerical calculations [see Fig. 4(b)].

It is interesting to compare the influence of the incidence angle on the intensity of the first plasmonic mode for different positions of the electron beam. Figure 5 depicts EELS maps of the first plasmonic mode for the cases (a) $\alpha = 0°, \beta = 0°$, (b) $\alpha = 46°, \beta = 0°$, and (c) $\alpha = 0°, \beta = 46°$. For a quantitative analysis, in Fig. 5(d) we show line scans along the x axis for $\alpha = 0°$ and $\alpha = 46°$ [see the dotted lines in Figs. 5(a) and 5(b), respectively]. Between the tips of the SRR, the intensity shows a strong dependence on α (see the discussion above). In contrast, the intensity hardly changes if the electron beam is located on one of the tips. A qualitative explanation for this behavior is that the electric field lines in the vicinity of the tips exhibit a radial character and thus always have a component parallel to the electron trajectory [see Fig. 2(b)]. This illustrates that we can use angular-resolved electron energy loss spectroscopy to obtain a qualitative understanding of the orientation of the electric field in the vicinity of a metallic nanostructure.

IV. CONCLUSION

We have performed angular-resolved electron energy loss spectroscopy in a scanning transmission electron microscope to investigate the plasmonic near field of a split-ring resonator. Our experiments demonstrate that probing a metallic nanostructure with an electron beam from different directions allows one to obtain a qualitative understanding of the local orientation of its plasmonic near field. In particular, we have shown that EELS is not, in general, blind to plasmonic hot spots in gap regions. Numerical calculations based on the DGTD method support the experimental findings.

ACKNOWLEDGMENTS

S.I. and S.L. acknowledge the financial support of the DFG-Project LI 1641/2-1. D.C.B. gratefully acknowledges funding through the National Science Foundation Awards (NSF No. 1040243 and NSF No. 1108382). F.v.C. acknowledges financial support by the DAAD.

[1] A. G. Brolo, Nat. Photonics **6**, 709 (2012).
[2] P. Bharadwaj, B. Deutsch, and L. Novotny, Adv. Opt. Photonics **1**, 438 (2009).
[3] M. Kauranen and A. V. Zayats, Nat. Photonics **6**, 737 (2012).
[4] M. S. Tame, K. R. McEnery, S. K. Özdemir, J. Lee, S. A. Maier, and M. S. Kim, Nat. Phys. **9**, 329 (2013).
[5] J. Nelayah, M. Kociak, O. Stéphan, F. J. García de Abajo, M. Tencé, L. Henrard, D. Taverna, I. Pastoriza-Santos, L. M. Liz-Marzán, and C. Colliex, Nat. Phys. **3**, 348 (2007).
[6] J. Nelayah, L. Gu, W. Sigle, C. T. Koch, I. Pastoriza-Santos, L. M. Liz-Marzán, and P. A. van Aken, Opt. Lett. **34**, 1003 (2009).
[7] M. Bosman, V. J. Keast, M. Watanabe, A. I. Maaroof, and M. B. Cortie, Nanotechnology **18**, 165505 (2007).
[8] D. Rossouw and G. A. Botton, Phys. Rev. Lett. **110**, 066801 (2013).
[9] A. L. Koh, K. Bao, I. Khan, W. E. Smith, G. Kothleitner, P. Nordlander, S. A. Maier, and D. W. McComb, ACS Nano **3**, 3015 (2009).
[10] M.-W. Chu, V. Myroshnychenko, C. H. Chen, J.-P. Deng, C.-Y. Mou, and F. J. García de Abajo, Nano Lett. **9**, 399 (2009).
[11] I. Alber, W. Sigle, S. Müller, R. Neumann, O. Picht, M. Rauber, P. A. van Aken, and M. E. Toimil-Molares, ACS Nano **5**, 9845 (2011).
[12] H. Duan, A. I. Fernández-Domínguez, M. Bosman, S. A. Maier, and J. K. W. Yang, Nano Lett. **12**, 1683 (2012).
[13] F.-P. Schmidt, H. Ditlbacher, U. Hohenester, A. Hohenau, F. Hofer, and J. R. Krenn, Nano Lett. **12**, 5780 (2012).
[14] G. Boudarham, N. Feth, V. Myroshnychenko, S. Linden, J. García de Abajo, M. Wegener, and M. Kociak, Phys. Rev. Lett. **105**, 255501 (2010).
[15] F. von Cube, S. Irsen, J. Niegemann, C. Matyssek, W. Hergert, K. Busch, and S. Linden, Opt. Mater. Express **1**, 1009 (2011).
[16] F. von Cube, S. Irsen, R. Diehl, J. Niegemann, K. Busch, and S. Linden, Nano Lett. **13**, 703 (2013).
[17] C. Diaz-Egea, W. Sigle, P. A. van Aken, and S. I. Molina, Nanoscale Res. Lett. **8**, 337 (2013).
[18] U. Hohenester, H. Ditlbacher, and J. R. Krenn, Phys. Rev. Lett. **103**, 106801 (2009).
[19] R. H. Ritchie, Phys. Rev. **106**, 874 (1957).
[20] F. J. García de Abajo and M. Kociak, Phys. Rev. Lett. **100**, 106804 (2008).
[21] F. J. García de Abajo, Rev. Mod. Phys. **82**, 209 (2010).
[22] A. Hörl, A. Trügler, and U. Hohenester, Phys. Rev. Lett. **111**, 076801 (2013).
[23] O. Nicoletti, F. de la Peña, R. K. Leary, D. J. Holland, C. Ducati, and P. A. Midgley, Nature (London) **502**, 80 (2013).
[24] M. W. Klein, C. Enkrich, M. Wegener, C. S. Soukoulis, and S. Linden, Opt. Lett. **31**, 1259 (2006).
[25] M. Husnik, F. von Cube, S. Irsen, S. Linden, J. Niegemann, K. Busch, and M. Wegener, Nanophotonics **2**, 241 (2013).
[26] K. Busch, M. König, and J. Niegemann, Laser Photonics Rev. **5**, 773 (2011).
[27] C. Matyssek, J. Niegemann, W. Hergert, and K. Busch, Photonics Nanostruct. Fundam. Appl. **9**, 367 (2011).